

MIMO-SAR Tomography

Gerhard Krieger, DLR, Microwaves and Radar Institute, gerhard.krieger@dlr.de, Germany

Tobias Rommel, DLR, Microwaves and Radar Institute, tobias.rommel@dlr.de, Germany

Alberto Moreira, DLR, Microwaves and Radar Institute, alberto.moreira@dlr.de, Germany

Abstract

MIMO SAR employs multiple transmit and receive channels to improve the imaging performance and to acquire novel geoinformation products. One example is SAR tomography, where the simultaneous transmission and reception with multiple antennas can provide a large number of baselines with a small number of antennas. In the limit, an appropriately designed MIMO-SAR configuration with N_{Tx} transmitters and N_{Rx} receivers can provide in total $N_{Tx} \cdot N_{Rx}$ independent phase centers and therefore $N_{Tx} \cdot N_{Rx} - 1$ independent baselines for SAR tomography. The other extreme is provided by uniform linear arrays with co-located transmitters and receivers. Such configurations are characterized by a large number of overlapping effective phase centers and are therefore regarded as highly redundant. In this paper, we will show that such a redundancy is nevertheless well suited to resolve an inherent challenge of conventional SAR tomography, which is limited in providing unambiguous 3-D scatterer position estimates in case of multiple scattering. For this, we show that redundant MIMO arrays allow not only an *a posteriori* beamforming on receive, but, at the same time, also a comparable *a posteriori* (i.e. after data acquisition) beamforming on transmit. This means that one can emulate, from one and the same recorded MIMO-SAR data set, different illumination scenarios on transmit and receive. By evaluating the 2-D spectrum provided by the independent Tx and Rx beams, it becomes then possible to differentiate between single- and multiple-bounce scattering. The separation between single- and double-bounce scattering has also been successfully demonstrated in a ground-based radar experiment and is presented in another EUSAR paper [16].

1 Introduction

Conventional SAR imaging implies a projection from the physical 3-D object space to a planar 2-D radar image where the image coordinates are range and azimuth. This means that a single image pixel contains the focused radar echoes from all elemental scatterers that are contained within a circular ring or torus centred on the platform path.¹ The radius of the torus is given by the measured range and its radial extent and width are provided by the range and azimuth resolutions, respectively. As a result, the elevation angle coordinates of the individual scatterers are lost, and a single SAR image contains therefore only very limited information about the 3-D structure of the imaged scene.

The objective of SAR tomography is to overcome this limitation and to provide a real 3-D imaging of semi-transparent volume scatterers like vegetation, dry soil, sand, and ice [1], [2]. SAR tomography has furthermore the potential to resolve distortions in radar images due to layover and foreshortening [3], [4]. The basic idea of SAR tomography is illustrated in Figure 1 which shows on the upper left multiple phase centres that form a sparse aperture perpendicular to the flight direction. The phase centres may represent the positions of real antennas or they may be virtual, as in the case of a multistatic MIMO SAR with multiple transmitters and receivers. By combining the signals from the phase centre positions, it becomes possible to form a set of narrow beams that provide additional information about the scatterer distribution in the elevation direction. This information is now well suited to divide the torus-shaped resolution cell from a conventional SAR acquisition into a set of smaller 3-D resolution cells. Assuming a sufficiently fine range resolution, it is then straightforward to compute the vertical

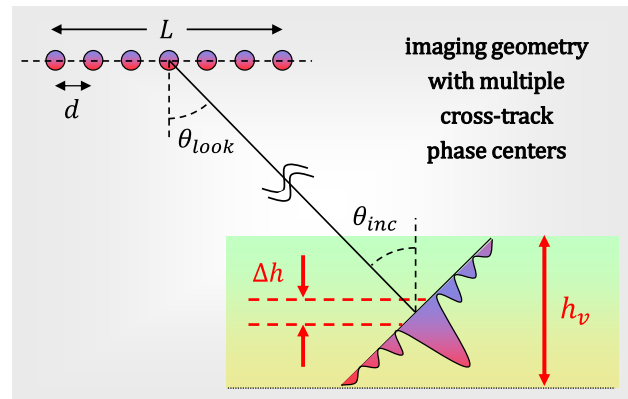


Figure 1: Illustration of SAR tomography. Multiple phase centres in the cross-track direction enable the formation of narrow beams that can be used to separate scatterers that fall in the same range resolution cell but are located at different elevation angles θ_{look} .

resolution Δh as

$$\Delta h \approx \frac{\lambda r_0 \sin \theta_{inc}}{m L \cos \theta_{look}} \quad (1)$$

where λ is the wavelength, r_0 the slant range, θ_{inc} the local incident angle, m a factor that is $m = 1$ for a bistatic single-pass formation and $m = 2$ for a monostatic repeat-pass configuration, θ_{look} the array look angle, and L the length of the virtual array (cf. Figure 1). Another parameter of interest is the height of ambiguity. Ambiguities in the tomographic measurements arise from grating lobes of the sparse array. Assuming a uniform arrangement of the antennas, the spacing between the grating lobes is determined by the separation between the virtual phase centres and it is again straightforward to compute the maximum volume height h_v that can be imaged without vertical aliasing as

$$h_v \approx \frac{\lambda r_0 \sin \theta_{inc}}{m d \cos \theta_{look}} \quad (2)$$

¹ This common view is only true for single scattering (first Born approximation). In case of multiple scattering, the corresponding objects may be located outside the torus. This will be discussed later in more detail and we will see that MIMO SAR offers interesting opportunities to separate single from multiple scattering.

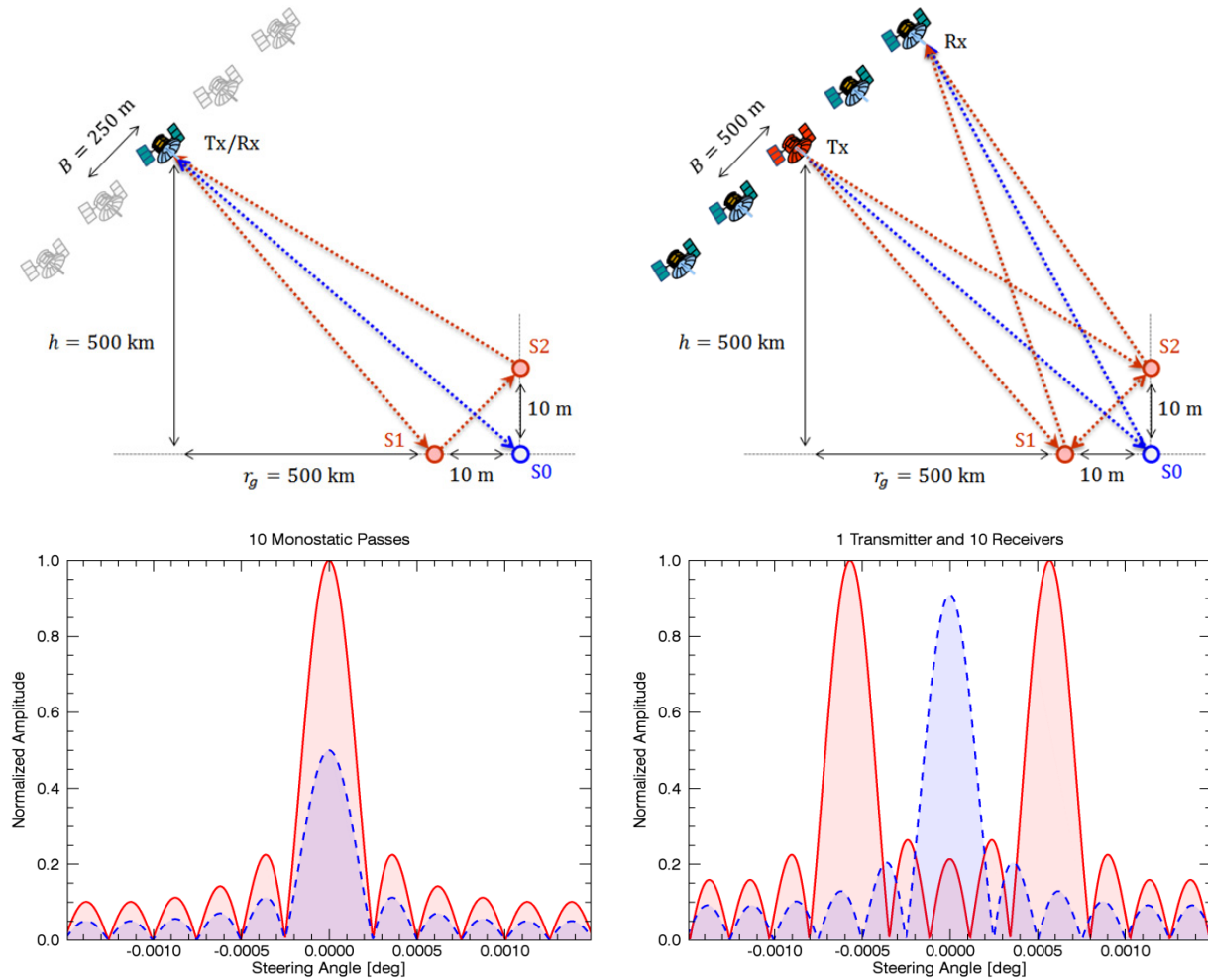


Figure 2: Comparison of monostatic repeat-pass (left) and multi-static single-pass (right) SAR tomography. The blue curves show the single-bounce response obtained for scatterer S0 ($Tx \rightarrow S0 \rightarrow Rx$). The red curves show the double bounce response for scatterers S1 and S2 ($Tx \rightarrow S1 \rightarrow S2 \rightarrow Rx$ and $Tx \rightarrow S2 \rightarrow S1 \rightarrow Rx$). Note the striking difference between the responses for the repeat-pass monostatic and the single-pass multistatic configurations in case of multiple scattering.

From Equation (1) it becomes clear that a large array extent L is required to obtain a good vertical resolution. On the other hand, Equation (2) reveals that a fine spacing between the phase centres is required to avoid height ambiguities. Assuming a uniformly spaced (real or virtual) antenna array, the number of required phase centres is easily computed from the ratio of the volume height h_v that should be imaged without ambiguities and the vertical resolution Δh as $N = h_v / \Delta h + 1$. Hence, a large number of phase centres is typically required.

2 Repeat- & Single-Pass Tomography

There exist three basic configurations to obtain the required number of baselines for SAR tomography:

- multi-pass tomography with a conventional monostatic SAR satellite,
- single-pass multistatic SAR tomography with one transmitter and N_{Rx} receiver satellites,
- single-pass MIMO-SAR tomography with N_{Tx} transmitters and N_{Rx} receivers.

A further option, to be discussed in more detail in Section 3, is the combination of several repeated single-pass acquisitions with varying baselines. To obtain a uniform framework for the analysis of the different configurations, they are often described in terms of their virtual phase centres

that shall provide a direct link between equivalent mono- and bistatic configurations [5], [6], [7], [8]. This simplified description neglects, however, some important differences which are analysed in more detail in Figure 2.

The upper left panel of Figure 2 illustrates a monostatic repeat-pass scenario where the scene is imaged by ten passes of a conventional SAR satellite. It is, moreover, assumed that the individual passes are uniformly separated by perpendicular baselines of 250 m. The upper right of Figure 2 shows, in contrast, a multistatic single-pass scenario, where the scene is illuminated by a single transmitter and the scattered signal is simultaneously recorded by 10 receivers that are mutually separated by perpendicular cross-track baselines of 500 m. According to classic theory, the two configurations are equivalent in terms of their virtual phase centre positions [5], [6], [7], [8].

For each of these two SAR configurations we consider now two scattering scenarios: the first contains a single scatterer S0 that is located on the ground (blue circle), while the second consists of a double-bounce configuration with scatterer positions S1 and S2 as indicated by the red circles. The signal path for the first scenario is simply given by $Tx \rightarrow S0 \rightarrow Rx$. For the second scenario, we have, from reciprocity, the two equivalent signal paths $Tx \rightarrow S1 \rightarrow S2 \rightarrow Rx$ and $Tx \rightarrow S2 \rightarrow S1 \rightarrow Rx$.

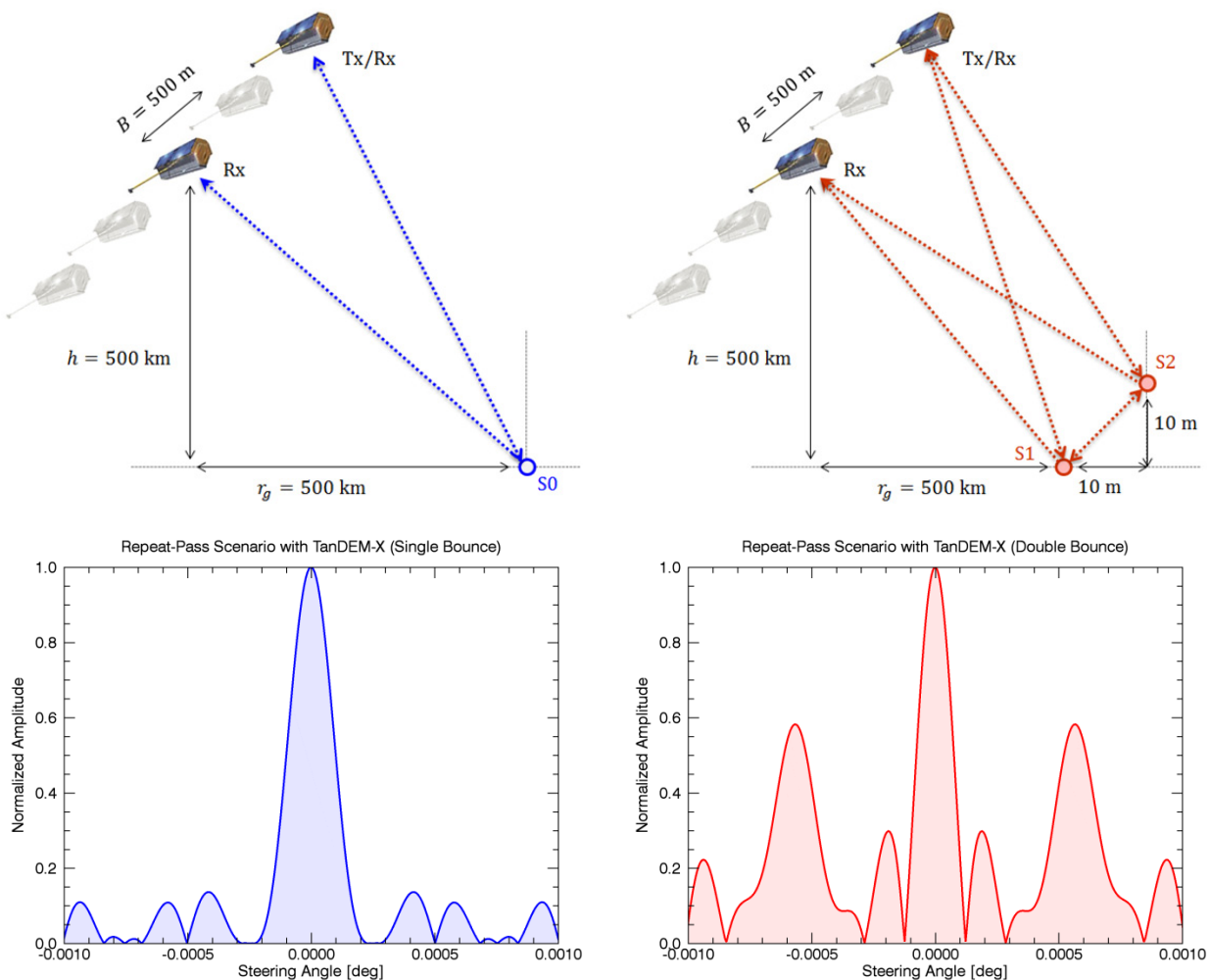


Figure 4: Comparison of single-bounce (left) and double-bounce (right) scattering scenarios for a TanDEM-X-like mixed single- and repeat-pass scenario. The upper row illustrates the acquisition scenario where the bistatic receiver (Rx) satellite is assumed to remain at the same central position for each pass and the combined transmitter and receiver (Tx/Rx) satellite systematically varies its position from pass to pass as indicated by the grey satellites. The blue dotted lines on the left indicated the ray paths from the Tx/Rx satellite to the single scatterer S0 and back to both receivers. The red dotted lines on the right illustrate the corresponding ray paths for the double bounce scattering scenario. The lower row shows for the single-bounce (left) and double-bounce (right) scattering scenarios the beamforming results where all available monostatic and bistatic data from 10 passes of the satellite formation have been employed with uniform amplitude weights.

The bottom of Figure 2 shows the corresponding results after tomographic processing, where we employed a straightforward beamformer in the elevation direction. It becomes evident from the left column of Figure 2 that the repeat-pass monostatic configuration yields, up to an irrelevant amplitude scaling, the same elevation-angle response for the single- and double-bounce scattering scenarios. This has been expected, as it is well known that the effective phase centre position for the double-bounce scattering from S1 and S2 is located at S0. The bistatic configuration, shown in the right column of Figure 2, yields for the single scatterer, again up to an irrelevant amplitude factor, the same response as in the monostatic case. For the double-bounce scattering, there are, however, striking differences between the single-pass and repeat-pass tomographic results: while the monostatic response is characterized by a single elevation lobe, the bistatic response shows now two different elevation lobes. This can be understood by the fact that the received radar echo (or scattered wave) has its origin always at the position of the last scatterer (i.e. S2 in case of $\text{Tx} \rightarrow \text{S1} \rightarrow \text{S2} \rightarrow \text{Rx}$ and S1 in case of $\text{Tx} \rightarrow \text{S2} \rightarrow \text{S1} \rightarrow \text{Rx}$), and the Rx beamformer therefore focuses always to this position. The presence of

two mutually displaced beamforming lobes from double-bounce-scattering may have annoying consequences for single-pass bistatic SAR tomography by disturbing the tomographic image as illustrated in Figure 3.

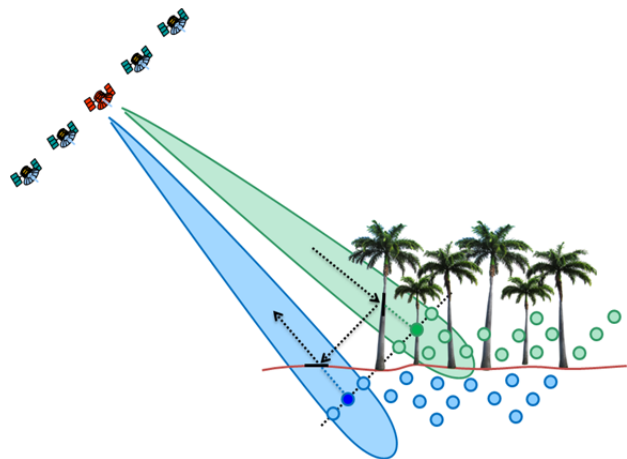


Figure 3: Single-pass tomography misinterprets the signals from double-bounce scattering as single-bounce scatterers below (blue dots) and above (green dots) the ground.

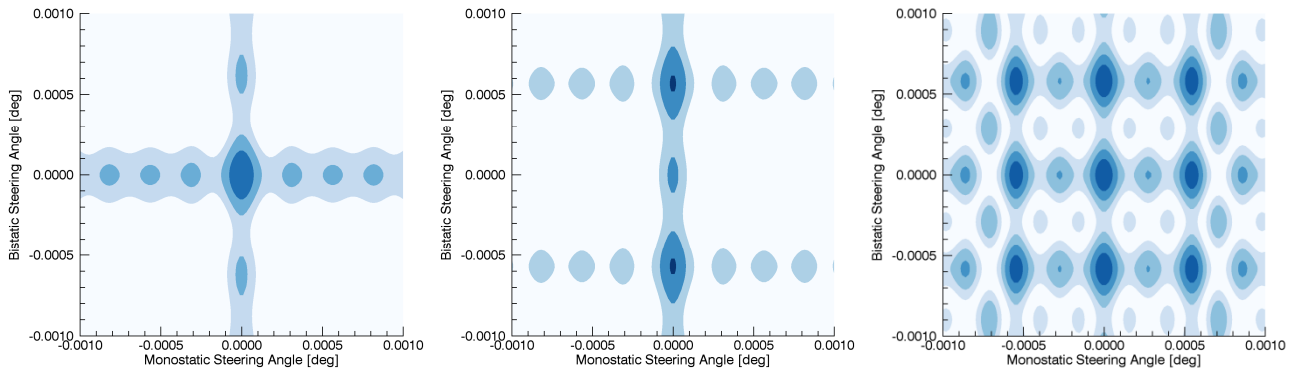


Figure 5: Results from a generalized 2-D mono-/bistatic beamformer for single-bounce scattering (left), double bounce scattering (middle), and a scenario with three single-bounce scatterers at the same range (right). The steering angles for the monostatic and bistatic data subsets are indicated on the horizontal and vertical axis, respectively.

3 Combination of Single-Pass and Repeat-Pass Acquisitions

In the previous section, we illustrated the striking differences that may arise between single-pass bistatic and repeat-pass monostatic tomograms in case of multiple scattering. Additional ambiguities may arise if the data from multiple passes of a bi- or multistatic satellite formation with multiple receivers and/or transmitters are combined to obtain a large number of virtual phase centres. While one can imagine a great variety of such configurations, we consider here for illustration a particularly simple scenario, where the formation consists of a single transmitter and two receivers. Such a scenario may, for example, arise in TanDEM-X or Tandem-L, where one satellite follows always the same orbital tube, while the second satellite is characterized by varying cross-track baselines [9], [10]. Figure 4 illustrates for such a scenario the corresponding beamforming results for the case of single- and double-bounce scattering. It becomes clear that the tomographic response from the double-bounce scattering scenario is now characterized by three ambiguous peaks that could also result from three individual single-bounce scatterers at different heights.

A possible approach to differentiate the two scenarios may be a separation of the monostatic and bistatic data into two disjoint sets. By forming for each of these sets a tomogram, one can explore the resulting product space and look for systematic differences between the monostatic and bistatic tomograms in case of single- and double-bounce scattering. One such example is illustrated in Figure 5 where we show the results of a generalized 2-D beamformer that steers the beams for the mono- and bistatic data to different directions as indicated by the horizontal and vertical axes. It becomes clear that the responses from single-bounce (left) and double-bounce (middle) scattering occupy different locations in the 2-D beamspace. The positions in the 2-D beamspace are, however, not unambiguously associated with single- and double-bounce scattering. This is illustrated in Figure 5 on the right, which shows the 2-D response for the case of three single-bounce scatterers that all have the same range as the scatterer S0, but slightly different elevation angles. We will show in the following that a MIMO SAR with multiple transmitters and receivers offers additional degrees of freedom that are well suited to unambiguously distinguish between single and multiple bounce scattering.

4 MIMO-SAR Tomography

It has often been emphasized that the employment of MIMO-SAR techniques offers the potential to provide a large number of virtual phase centres with a limited number of transmitters and receivers [11], [12]. For example, an appropriately designed MIMO-SAR satellite formation with three transmitters and five receivers could provide, in a single pass, a vertical resolution of $\Delta h = 5$ m for a height of ambiguity of $h_v = 70$ m. In case of structured scattering environments, which may, for example, arise from distinct vertical layers in forests or sparse scatterer densities in urban areas, the height resolution could be further improved by employing, for example, dedicated spectral estimation or compressive sensing techniques [13], [14].

Beyond these obvious advantages for the cost-efficient implementation of a spaceborne single-pass tomographic radar system, MIMO SAR offers another and somewhat complementary opportunity for SAR tomography. For this, we consider a MIMO-SAR configuration that forms a uniform linear array of co-located Tx and Rx antennas as illustrated on the upper left of Figure 6. On the first sight, such an arrangement may seem as a waste of system resources, since it generates a large number of virtual phase centres

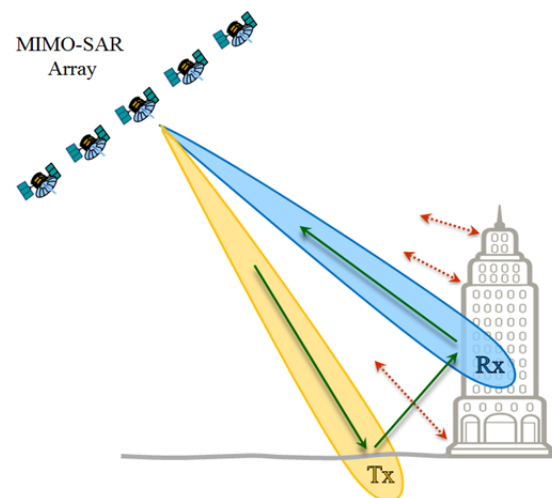


Figure 6: MIMO SAR provides full control over the shape and direction of the Tx and Rx beams after signal reception. Such *a posteriori* beamforming can, for example, be used for the separation of different scattering mechanisms in natural and artificial environments.

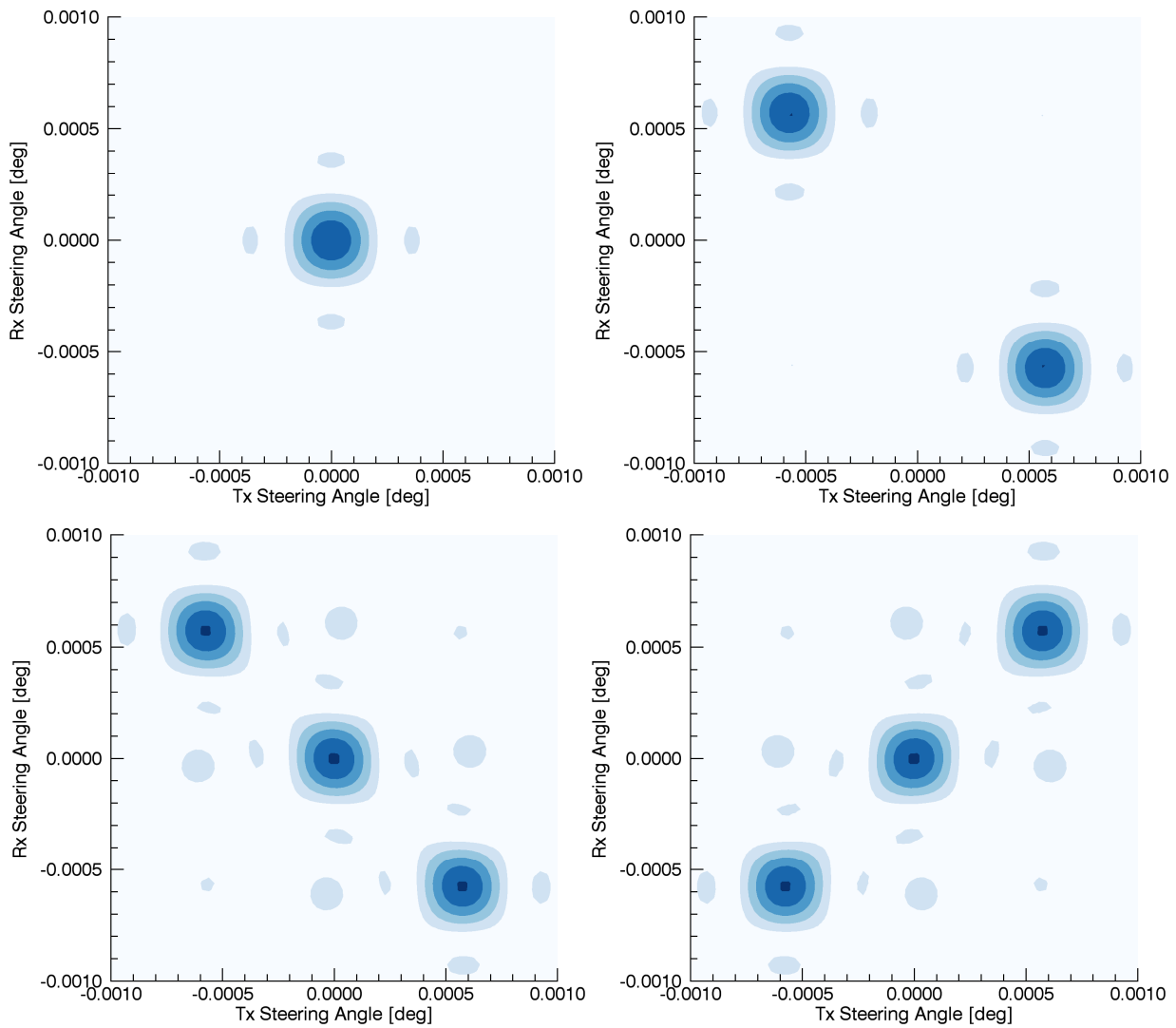


Figure 7: MIMO-SAR tomography with distinct Tx and Rx beams for different scattering scenarios. The upper left plot shows the generalized 2-D Tx/Rx beamformer response for the single-bounce scatterer S0 illustrated by the blue dot in Figure 2. The upper right plot shows the corresponding double-bounce response from S1 and S2 where the upper left response represents the ray path $Tx \rightarrow S1 \rightarrow S2 \rightarrow Rx$, and the lower right response represents $Tx \rightarrow S2 \rightarrow S1 \rightarrow Rx$. The lower left plot illustrates the response for the combined single-bounce and double-bounce scattering scenario from Figure 2. The lower right plot illustrates, for comparison, the response for three single-bounce scatterers that have all the same range, but different elevation angles. The results demonstrate the capability of MIMO-SAR tomography to unambiguously differentiate between different scattering mechanisms.

that are coincident and therefore regarded as "redundant" in almost every MIMO-SAR publication. As before, we further assume that the echoes from the multiple transmitters can be well separated within each receiver. This may, for example, be achieved by simultaneously transmitting mutually short-term shift-orthogonal (STSO) waveforms from the different transmitters and applying a set of appropriate space-time filters to the recorded radar signals within each receiver [15]. By this, one gets, for each receiver, N_{Tx} independent SAR images out of its recorded radar echoes. By combining these N_{Tx} image signals in a linear beamformer, one can, from one and the same recorded data set, emulate a wide spectrum of illumination scenarios that range from the wide beam radiation pattern of a single transmitter to a highly advanced Tx beamforming where sharp nulls are formed in some desired directions. Note that this *a posteriori* Tx beamforming is completely independent from any Rx beamforming that would involve the combination of the radar signals from multiple receivers.

One interesting application scenario for the separate Tx and Rx beamforming with a colocated MIMO-SAR array is illustrated in Figure 6. Here, a narrow transmit beam is formed for each receiver by a linear superposition of the separated signals from the multiple transmitters. We next assume that the emulated Tx beams of all receivers are steered to the same point, which is in this example located on the left hand side of the house. By combining the signals from the multiple receivers, one can again form a narrow Rx beam. The classical approach would be to steer the Rx beam to the same direction as the Tx beam. An interesting option arises, however, for the case where the virtual Rx beam is steered to a direction that is different from that of the virtual Tx beam. Assuming that the two beams have no mutual overlap, all radar echoes from single-bounce scattering will be suppressed, since either the scatterer is outside the Tx beam and therefore not illuminated, or the radar echo arrives from a direction that is not covered by the Rx beam. By this, it becomes, for example, possible to separate single-bounce scattering from multiple-bounce scattering.

A systematic variation of the Tx and Rx beams opens now an $(N_{Tx} \cdot N_{Rx})$ -dimensional observation space that can be used for the analysis and separation of different scattering mechanisms in both natural and artificial environments. A simple example for such an analysis is illustrated in Figure 7, which shows the results of a generalized 2-D Tx/Rx beamformer for different single- and double-bounce scattering scenarios. The upper left and upper right plots show the individual responses for the single- and double-bounce scattering scenarios of Figure 2, respectively, while the lower left plot shows the response to a joint single- and double-bounce scattering scenario. The lower right plot illustrates, for comparison, the generalized 2-D Tx/Rx beamformer result for the case of three single-bounce scatterers that are all located at the same range, but at slightly different elevation angles with respect to the MIMO-SAR satellite formation.

For a discussion of the results, recall that the scenario of Figure 2 contained a single-bounce scattering from S0, and a double-bounce scattering from S1 and S2. The single-bounce scattering from S0 is clearly visible in the centre of the generalized 2-D Tx/Rx beamformer results, where the transmit and receive beams are jointly steered to 0° . On the other hand, the double bounce response from $Tx \rightarrow S1 \rightarrow S2 \rightarrow Rx$ is visible in the upper left by steering the Tx beam to -0.006° and the Rx beam to $+0.006^\circ$. Vice versa, the double bounce response from $Tx \rightarrow S2 \rightarrow S1 \rightarrow Rx$ is visible in the lower right by steering the Tx beam to $+0.006^\circ$ and the Rx beam to -0.006° . In contrast, the two additional single-bounce scatterers, which are only present in the lower right plot of Figure 7, are clearly identified by steering the Tx and Rx beams jointly to either -0.006° or $+0.006^\circ$. From these results, it becomes evident that the 2-D MIMO-SAR tomograms in Figure 7 preserve the difference between single- and double-bounce scattering, and, as opposed to Figure 5, no mixing occurs between these two scattering mechanisms.

5 Discussion

Conventional SAR tomography is implicitly based on the first-order Born approximation. This neglects multiple scattering and can therefore cause scatterer mislocations and/or distortions in the tomogram, as illustrated in the simple example of Section 2. Building up on this observation, it has been shown that MIMO-SAR tomography offers the opportunity to gain additional information in complex scattering scenarios and to resolve ambiguities from multiple scattering. Further information can be obtained by combining MIMO-SAR tomography with a fully polarimetric mode which further extends the information space and is also well suited to separate single- from double-bounce scattering. The combination of MIMO-SAR tomography with SAR polarimetry promises therefore high potential for the analysis of complex three-dimensional scattering scenarios.

To prove some of the ideas put forward in this paper, a dedicated experiment has been performed by employing a ground-based MIMO demonstrator within an artificial environment that contained an appropriate arrangement of both single- and double-bounce scatterers. The preliminary results of this experiment confirm the ideas put forward in this paper and are presented in an accompanying paper [16].

References

- [1] A. Reigber and A. Moreira, "First demonstration of airborne SAR tomography using multibaseline L-band data," *IEEE Transactions on Geoscience and Remote Sensing*, Vol. 38, No. 5, pp. 2142–2152, 2000.
- [2] S. Tebaldini, "Single and multipolarimetric SAR tomography of forested areas: A parametric approach," *IEEE Transactions on Geoscience and Remote Sensing*, Vol. 48, No. 5, pp. 2375–2387, 2010.
- [3] F. Gini, F. Lombardini, and M. Montanari, "Layover solution in multibaseline SAR interferometry," *IEEE Transactions on Aerospace and Electronic Systems*, Vol. 38, No. 4, pp. 1344–1356, 2002.
- [4] X. Xiang Zhu and R. Bamler, "Very high resolution spaceborne SAR tomography in urban environment," *IEEE Transactions on Geoscience and Remote Sensing*, 48(12):4296–4308, 2010.
- [5] R.C. Heimiller, J.E. Belyea, and P.G. Tomlinson, "Distributed array radar," *IEEE Transactions on Aerospace Electronic Systems*, Vol. 19, pp. 831–839, 1983.
- [6] R. T. Hoftor and S. A. Kassam, "The unifying role of the coarray in aperture synthesis for coherent and incoherent imaging," *Proceedings of the IEEE*, Vol. 78, No. 4, pp. 735–752, April 1990.
- [7] J. Ender, "MIMO-SAR," In *Proc. International Radar Symposium*, pp. 667–674, Cologne, Germany, 2007.
- [8] D. Cristallini, D. Pastina, and P. Lombardo, "Exploiting MIMO SAR potentialities with efficient cross-track constellation configurations for improved range resolution," *IEEE Transactions on Geoscience and Remote Sensing*, Vol. 49, No. 1, pp. 38–52, 2011.
- [9] G. Krieger, M. Zink, M. Bachmann, B. Bräutigam, D. Schulze, M. Martone, et al., "TanDEM-X: a radar interferometer with two formation flying satellites," *Acta Astronautica*, Vol. 89, pp. 83–98, 2013.
- [10] A. Moreira, G. Krieger, I. Hajnsek, et al., "Tandem-L: A highly innovative bistatic SAR mission for global observation of dynamic processes on the Earth's surface," *IEEE Geoscience and Remote Sensing Magazine*, Vol. 3, No. 2, pp. 8–23, June 2015.
- [11] G. Krieger, J. Mittermayer, S. Buckreu, M. Wendler, T. Sutor, F. Witte, and A. Moreira, "Sector imaging radar for enhanced vision," *Aerosp. Sci. Technol.*, Vol. 7, No. 2, pp. 147–158, Mar. 2003.
- [12] J. Klare, A. Brenner, and J. Ender, "A new airborne radar for 3D imaging - image formation using the ARTINO principle. In *Proc. European Conference on Synthetic Aperture Radar (EUSAR)*, Dresden, Germany, 2006.
- [13] F. Lombardini and A. Reigber, "Adaptive spectral estimation for multibaseline SAR tomography with airborne L-band data," In *Proc. IEEE Int. Geoscience and Remote Sensing Symposium (IGARSS)*, pp. 2014–2016, Toulouse, France, 21–25 July 2003.
- [14] X. Xiang Zhu and R. Bamler, "Super-resolution power and robustness of compressive sensing for spectral estimation with application to spaceborne tomographic SAR," *IEEE Transactions on Geoscience and Remote Sensing*, Vol. 50, No. 1, pp. 247–258, 2012.
- [15] G. Krieger, "MIMO-SAR: Opportunities and Pitfalls," *IEEE Transactions on Geoscience and Remote Sensing*, Vol. 52, No. 5, pp. 2628–2645, May 2014.
- [16] T. Rommel and G. Krieger, "Detection of Multipath Propagation Effects in SAR-Tomography with MIMO Modes", paper accepted for EUSAR 2016.